ISIJ International, Vol. 39 (1999), No. 12, pp. 1270–1279

Solidification Phase and Microstructure Selection Maps for Fe–Cr–Ni Alloys

Shigeo FUKUMOTO and Wilfried KURZ[1)]

Formerly Swiss Federal Institute of Technology Lausanne (EPFL). Now at Hikari R & D Laboratory, Nippon Steel Corporation, Shimata, Hikari, Yamaguchi-ken, 743 Japan. 1) Department of Materials, Swiss Federal Institute of Technology Lausanne (EPFL), 1015 Lausanne, Switzerland.

(Received on June 14, 1999; accepted in final form on August 16, 1999)

Directional solidification and laser experiments have been performed in Fe–18.0%Cr–Ni alloys to evaluate the effects of alloy composition and growth velocity on microstructure and phase selection. Solidification microstructure selection maps are described by microstructure (dendrite/cell, plane front and eutectic) models and compared with experimental results. Theoretical predictions are in good agreement with experimental results. It demonstrates the potential of this approach to analyze the microstructure and phase formation.

KEY WORDS: dendrite; eutectic; banding; laser treatment; directional solidification; Fe–Cr–Ni alloy; phase/microstructure selection; microstructure map.

1. Introduction

Hot cracking during welding is a critical problem for Cr–Ni stainless steels. It is well known that this phenomenon is caused by microsegregation of trace elements such as P, S during solidification of austenite (γ). The susceptibility to hot cracking can be minimized by inducing a certain amount of δ-ferrite in the as-welded microstructure.[1–3)] Usually solidification microstructures in austenitic stainless steels are determined by the composition. The composition balance between ferrite stabilizing elements and austenite stabilizing elements (*i.e.*, Cr/Ni-equivalent) is used to predict the solidification microstructures such as residual δ-ferrite content[4–6)] and the solidification modes.[7,8)] The phase transition from stable δ to metastable γ as primary solidification phase has also been observed with increasing solidification velocity.[9–16)] Related to this, an increase of the hot cracking tendency has been predicted for laser and electron beam welding.[17,18)] Therefore, phase selection in austenitic stainless steels is of great technical importance.

Several authors have studied microstructure/phase selection during weld solidification in austenitic stainless steels and Fe–Cr–Ni alloys. Suutala[9)] examined the effects of composition and growth velocity on the δ to γ transition in austenitic stainless steels during gas tungsten arc (GTA) welding and compared it with previous work. It has been suggested that the critical values of Cr/Ni-equivalent[8)] corresponding to the δ to γ transition gradually increased with an increase of growth velocity.[18)] Nakao *et al.*[12)] classified the solidification morphologies of Fe–Cr–Ni alloys during laser treatment into six types of microstructures and the effect of cooling rate on solidification modes was investigated. Elmer *et al.*[13)] evaluated the solidification microstructure in Fe–Cr–Ni alloys (Fe$\cong$55%) in electron beam remelting experiments. The primary phase and microstructural morphologies which resulted from solidification and subsequent δ/γ transformation were classified according to electron beam scanning speed and composition. Bobadilla *et al.*[19)] studied the effects of composition and solidification rate on the solidification mode (primary δ or γ) of austenitic stainless steels. The transition from stable δ to metastable γ dendrites was explained by dendrite growth theory. The present authors[15,16)] investigated the phase selection during laser treatment in ternary Fe–Cr–Ni alloys (Cr$\cong$18%) and in multicomponent stainless steels. As in the work by Bobadilla *et al.*, it was theoretically shown that the transition from δ to γ is controlled by the dendrite growth kinetics.

Preferential solidification of γ in hypereutectic (primary δ) Fe–Cr–Ni alloys has been also studied in chill casting by several authors.[48,49)] The formation of metastable γ was observed at the chill surface. Through the temperature measurements of melts at the chill, Mizukami *et al.*[48)] found that the solidification at the chill occurred into the substantially undercooled melt. Phase transition was successfully analyzed by the model of free dendrite growth with a negative temperature gradient. Koseki–Flemings[49)] proposed a phase stability mechanism, in which δ phase massively transformed to γ in the early stage of solidification so that γ grew without competition, for the explanation of the δ to γ transition during the chill casing of the undercooled melts. On the other hand, metastable δ solidification in hypoeutectic

(primary γ) Fe–Cr–Ni alloys has been investigated during levitation melting and solidification by several authors.[50-52] It was concluded that the phase selection was controlled at the nucleation stage due to the ease of δ nucleation from the undercooled melts.

Moreover, several kinds of solidification microstructures have been observed for many alloys. In the case of Cr–Ni stainless steels, featureless microstructures which are characterized by compositional homogeneity have been observed at high growth rates.[11-13,20] These structures are considered to be due to single phase plane front solidification ($L \rightarrow \delta$ or γ) or massive transformation ($\delta \rightarrow \gamma$) which is mainly observed in fully ferrite solidification mode. Eutectic structures were also observed in Fe–Cr–Ni alloys during laser treatment with the high cooling rates[12] and during directional solidification[21] at low velocities. In addition, a banded structure in which two microstructures (planar front and dendritic/cellular) form alternately parallel to the interface have been found at high velocities in the regime between cellular/dendritic and planar front solidification for several alloy systems.[22-24]

A general dendrite growth model has been developed for directional solidification including rapid solidification conditions.[25] Models extended to multicomponent systems have been published by several authors.[19,26,27] Moreover, microstructure modeling has been recently expanded into the description of solidification microstructure selection maps.[27-30] These diagrams indicate the microstructures (plane front, dendrite/cell, eutectic and bands) which results from growth competition between several microstructural morphologies of both stable and metastable phases. In these studies, good agreements between experimental results and theoretical predictions are obtained. Solidification microstructure selection maps are thus useful tools to control the quality of products and to optimize the solidification processes.

The aim of this study is to produce a solidification phase and microstructure selection map for a wide range of solidification velocities and temperature gradients in Fe–Cr–Ni alloys which form the basis of austenitic stainless steels. The present work is concentrated on the microstructure/phase selection under constrained (directional) growth conditions, *i.e.* with a positive temperature gradient. In this paper, some experimental results which were formerly obtained by laser welding experiment[15] are used to describe the δ to γ transition at medium growth rates. Laser experiments at the high and low velocity ranges and directional solidification experiments for the low growth rates were carried out in this work to evaluate the effects of composition and growth velocity on the phase and microstructure selection. Calculated solidification microstructure selection maps based upon theory were compared with experimental results.

2. Experimental Procedure

2.1. Alloys

Four alloys (alloy A, B, C and E) were prepared for the experiments. Pure iron (99.98%), chromium (99.995%) and nickel (99.98%) were melted using a HF induction furnace and cast into a copper mold under Argon atmosphere. **Figure 1** shows the ternary phase diagrams[31] in which the compositions of the alloys are also indicated. **Table 1** shows the chemical compositions and Cr/Ni ratios of the four alloys (all concentrations are in mass%). The chromium contents in the four alloys were 18.0 ± 0.1% and the nickel contents were 9.9 (A), 13.8 (B), 11.3 (C) and 11.5 (E)%, respectively. Alloy A, C and E solidify as primary ferrite and Alloy B solidifies as primary austenite according to the equilibrium diagram used. Alloy E was used for the Bridgman experiments and the other alloys were used for the laser experiments.

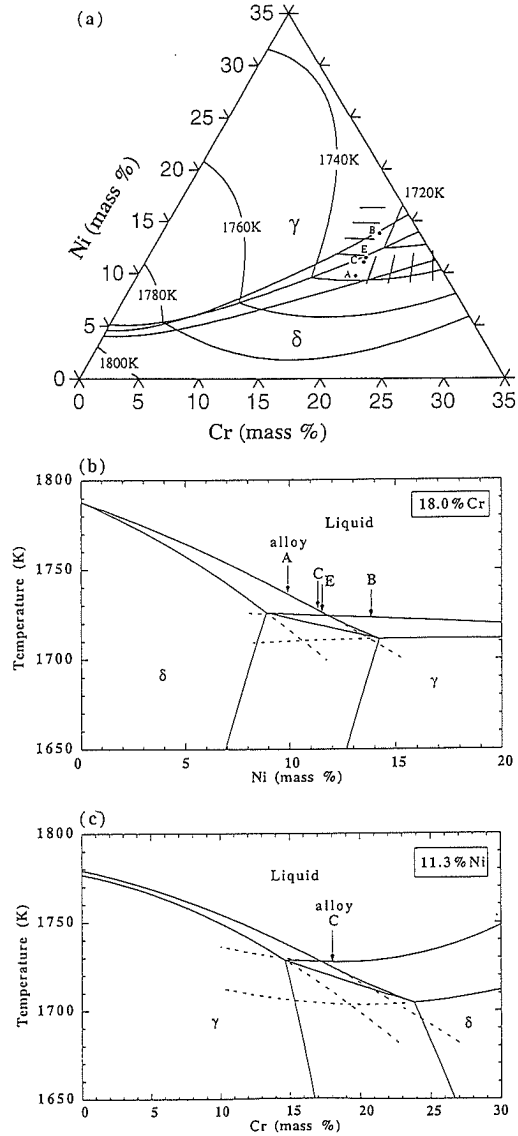

Fig. 1. The Fe–Cr–Ni phase diagrams with indications of the compositions of the four alloys used in this work. (a) ternary phase diagram including liquidus surface, tie lines for δ and γ solidification and line of two-fold saturation, (b) vertical section at 18% Cr including metastable liquidus and solidus lines relevant for δ-solidification and (c) vertical section at 11.3% Ni including metastable liquidus and solidus lines relevant for γ-solidification.

Table 1. Chemical composition of alloys in mass%.

	Fe	Cr	Ni	C	Si	Mn	P	S	Mo	N	O	Cr/Ni
Alloy A	Bal.	18.1	9.9	0.003	<0.05	<0.05	<0.008	<0.001	<0.02	0.0014	0.0132	1.83
Alloy B	Bal.	17.9	13.8	0.003	<0.05	<0.05	<0.008	<0.001	<0.02	0.0005	0.0144	1.30
Alloy C	Bal.	18.0	11.3	0.003	<0.05	<0.05	<0.008	<0.001	<0.02	0.0005	0.0130	1.59
Alloy E	Bal.	17.9	11.5	0.003	<0.05	<0.05	<0.008	<0.001	<0.02	0.0005	0.0151	1.56

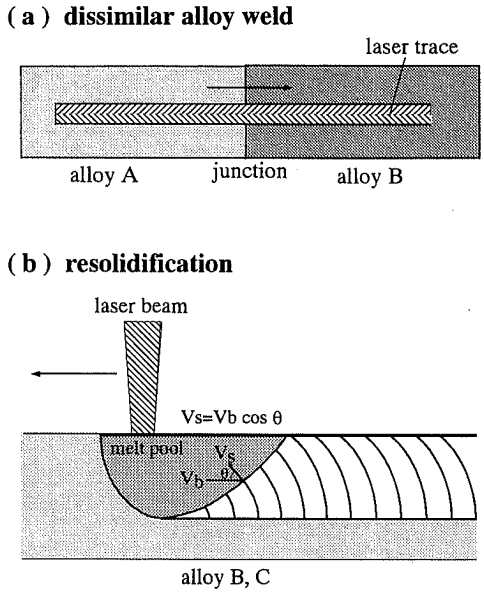

Fig. 2. Schematic of laser experiments: (a) dissimilar alloy weld and (b) resolidification.

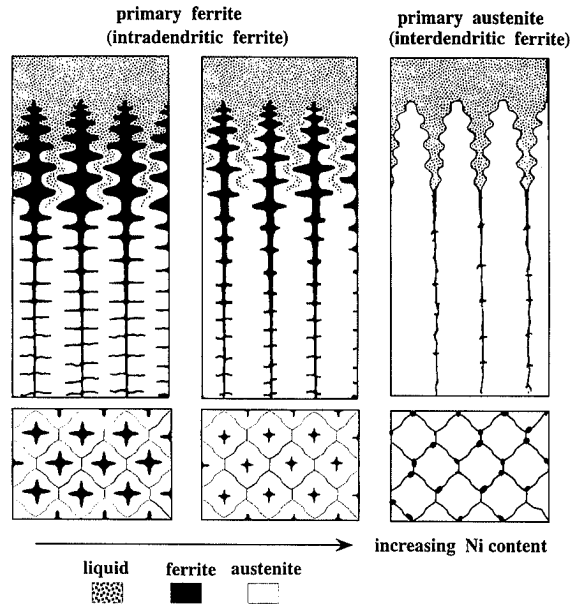

Fig. 3. Schematic representation of microstructural transitions during growth of different alloys (after Brooks and Thompson[3]).

2.2. Directional Solidification

Directional solidification experiments in a Bridgman apparatus were performed with alloy E. The furnace consists of a molybdenum susceptor heated by a high frequency induction coil and a liquid metal cooling device. An as-cast rod was contained in an alumina tube (4 mm internal diameter). After the initial melting and temperature stabilization under controlled Argon atmosphere, the crucible was lowered through the susceptor at a constant velocity ranging from 1.7 to 1 000 μm/s. At the end of the experiment, the tube was dropped into the liquid metal bath (eutectic Ga–In–Sn) in order to maximize the quench effect at the liquid/solid interface.

2.3. Laser Treatment

Laser treatments as shown in **Fig. 2** were carried out with a 1.7 kW continuous wave CO_2 laser. Microstructural transitions were observed by (a) changing the composition over distance in dissimilar alloy welds[20] at constant V_s and (b) increasing local solidification velocity in resolidification experiments at constant C_0.

In dissimilar alloy welds, two different materials (alloy A with low Ni content and alloy B with high Ni content) were used. The welds were made from alloys A and B with laser scanning speeds of 1, 5, 10, 15, 50 mm/s in order to evaluate the δ to γ transition. In simple resolidification experiments, the specimens of alloy B and C were remelted at different but constant laser scanning speeds ranging from 0.2 to 1 mm/s and the specimens of alloy B were remelted with constant laser scanning speeds ranging from 100 to 300 mm/s.

The specimens of dissimilar alloy welds and those of the resolidification experiments at low velocities were preheated by induction to 1 273 K in order to avoid growth instability due to the Marangoni effect,[22] which occurs especially at low velocities. The preheating technique was used for these series of experiments to produce the same level of thermal gradient. At the end of the experiments, the laser was turned off and specimens were quenched by pouring liquid tin or blowing Helium gas over them in order to achieve rapid cooling.

In this work, the local solidification velocity V_s was evaluated at the surface of the remelted zone. The growth velocity was determined by the scanning speed (V_b) and the angle (θ) between the scanning direction and the direction of interfacial motion evaluated through the form of the liquid pool at the surface of the specimen (*i.e.*, $V_s = V_b \cos\theta$). This procedure is acceptable if the dendrite growth axis lies in the surface.

2.4. Metallographic Analysis

Optical metallographic observations were carried out after polishing and electrolytical etching in 10% oxalic acid. The solidification modes are distinguished by the microscopic morphology and location of residual δ-ferrite[3,13] as shown schematically in **Fig. 3**. If ferrite (dark/gray phase) is found at dendrite/cell cores, the alloy solidified as primary ferrite which transforms partially into γ (bright/white phase) as the temperature drops. On the other hand, if the ferrite is present in the

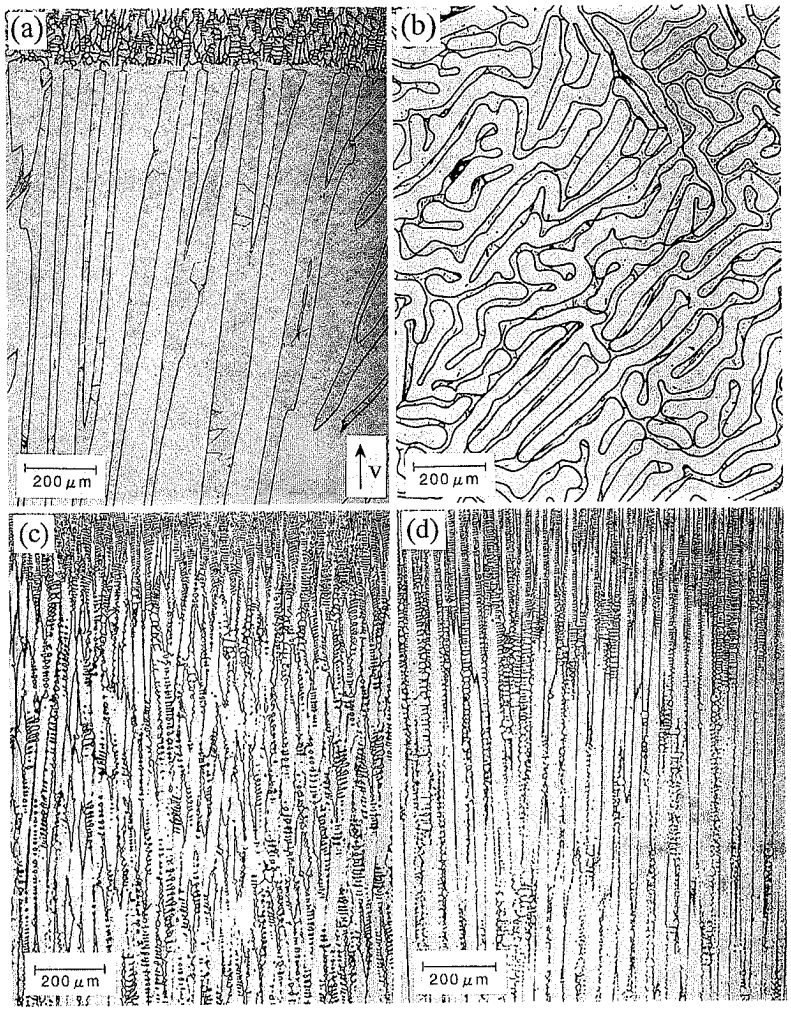

Fig. 4. Microstructures obtained by the Bridgman experiments of alloy E. (a) longitudinal section of eutectic structure at $V_s = 1.7\,\mu m/s$, (b) cross section (1.5 mm behind the solid/liquid interface) of eutectic structure at $V_s = 1.7\,\mu m/s$, (c) stable δ-dendrites at $V_s = 400\,\mu m/s$ and (d) metastable γ-dendrites at $V_s = 1000\,\mu m/s$. Gray phase is ferrite, white phase is austenite, respectively.

interdendritic regions, the alloy solidified as primary austenite.

Lamellar spacing measurements of the eutectic structure were made by taking 20 to 25 measurements of the 10 smallest values in cross sections closely behind the quenched solid–liquid interface.

Scanning electron microscopy (SEM) was also used to observe the fine microstructures. Microprobe analysis was made on the samples of the dissimilar alloy welds in order to evaluate the mean composition at the microstructural transition over a scanned area of approximately 0.1×0.4 mm. The concentration profile of Cr and Ni in the Bridgman experiments was also measured by stepwise spot analysis.

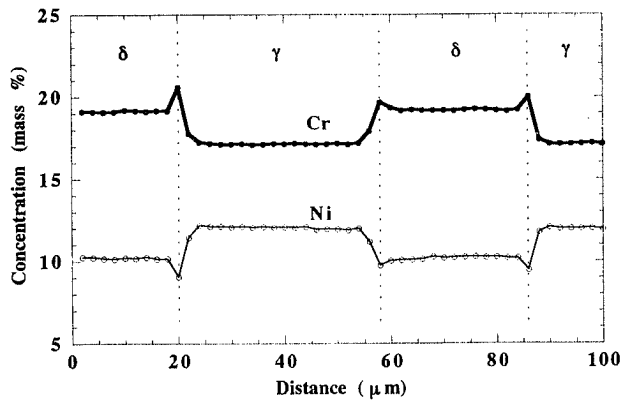

Fig. 5. Measured distribution of Cr and Ni across the eutectic structure in specimen E with $V_s = 1.7\,\mu m/s$.

3. Experimental Results

3.1. Directional Solidification (Alloy E)

Figure 4 shows typical microstructures obtained in the Bridgman experiments. In these photographs, the dark and bright parts respectively indicate ferrite (δ) and austenite (γ). At low velocities, simultaneous two phase growth was observed in the form of an irregular eutectic structure with a lamellar morphology. The measured average lamellar spacing near the quenched interface is $\lambda = 63\,\mu m$ at $V_s = 1.7\,\mu m/s$ and $\lambda = 26\,\mu m$ at $V_s = 8.0\,\mu m/s$. The distributions of Cr and Ni just below the solid/liquid interface of the eutectic-like structure is shown in **Fig. 5**. The measured concentration of Cr and Ni is fairly uniform at the center of the lamellar. However, an increase in Cr and a decrease in Ni within the lamellar boundaries was observed.

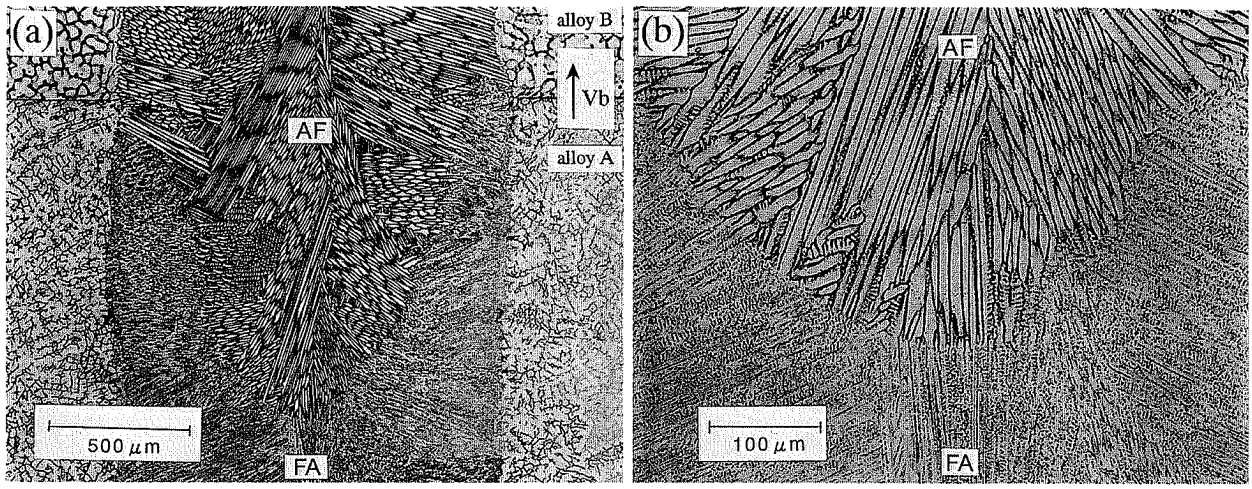

Fig. 6. Microstructural transitions from δ-dendrites to γ-cells/dendrites observed on the surface of a dissimilar (A–B) alloy welds at $V_b = 5$ mm/s. (b) shows the structure from (a) at four times higher magnification. "FA" indicates primary ferrite with secondary austenite and "AF" indicates primary austenite with secondary ferrite.

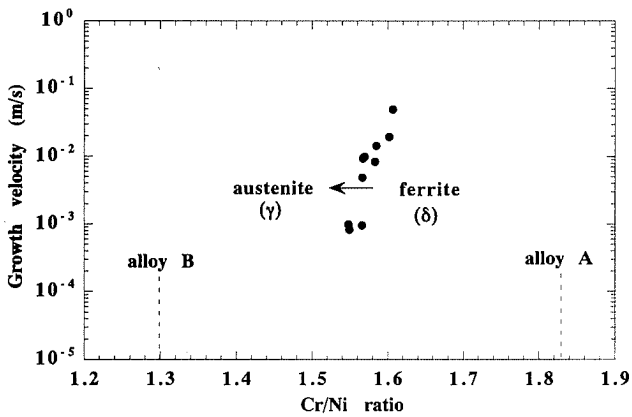

Fig. 7. Experimental results on phase selection in dissimilar alloy welds. The δ to γ transition with decreasing Cr/Ni ratio (alloy A → B) is shown as obtained from the local conditions of the melt pools of five specimens with the scanning velocities $V_b = 1$, 5, 10, 15, 50 mm/s.

Dendrites of stable δ phase were observed at medium growth rates ($V_s = 400\,\mu$m/s) as shown in Fig. 4(c). Residual δ-ferrite resulting from primary ferrite solidification and subsequent δ/γ transformation was found at dendrite cores. Metastable γ-dendrites were observed at high velocity ($V_s = 1\,000\,\mu$m/s) as shown in Fig. 4(d). It indicates that metastable γ-dendrites form preferably at high growth velocity.

3.2. Laser Treatment

An example of the δ to γ transitions obtained in dissimilar alloy welds is shown in Fig. 6. Alloy A solidified as primary ferrite and alloy B solidified as primary austenite in as-cast ingots as can be seen on the sides of the laser trace in **Fig. 6(a)**. The solidification modes in these pictures are classified into FA mode (primary ferrite with secondary austenite) and AF mode (primary austenite with secondary ferrite).[13,32] An abrupt transition from δ to γ was clearly observed. The effect of growth velocity and composition as measured along the transition front on the phase selection are given in **Fig. 7**. With a decrease in Cr/Ni ratio or an increase in growth velocity, metastable austenite forms preferably.

Figure 8 shows an eutectic microstructure as obtained in resolidification experiments of alloy C at $V_b = 0.2$ mm/s. Mainly rod-like eutectic structures were observed. Measured average spacings were less than 10 μm.

Figure 9 shows microstructures in the resolidification experiments of alloy B. γ-cells were observed in the lower velocity range as shown in Fig. 9(a). With increasing velocity, a banded structure, oscillating between γ-cellular growth and γ-plane front growth parallel to the solid–liquid interface appeared at the center of the laser trace as seen in Fig. 9(b). Microstructural transition from cellular to banded structure occurred in the range of $60 < V_s < 90$ mm/s.

4. Discussion

After a discussion of processing conditions and microstructure selection models, the growth of specific microstructures and corresponding maps will be presented.

4.1. Growth Rate and Temperature Gradient

The two process variables which influence the microstructure selection directly are growth rate (V_s) and temperature gradient (G). V_s has been determined by the relationship of Fig. 2(b) for laser experiments. The deviations of growth velocities are approximately $\pm 20\%$ in this work. In steady state Bridgman experiments $V_s = V_{crucible}$. The temperature gradient in the laser experiments can be obtained from numerical modeling[33] or calculated from the growth velocity and the cooling rate (ε) estimated by dendrite arm spacing measurements (*i.e.*, $G = \varepsilon / V_s$).[34] The absorption coefficient is needed to carry out the heat-flow simulation. As it could not be measured in the laser experiments with preheating, the latter method using the relationship between cooling rate and dendrite arm spacing evaluated by Esaka *et al.*[35] was applied. Assessed temperature gradient is 690 ± 150 K/mm at $V_s = 1$ mm/s. (Hunziker and Kurz[29] optimized

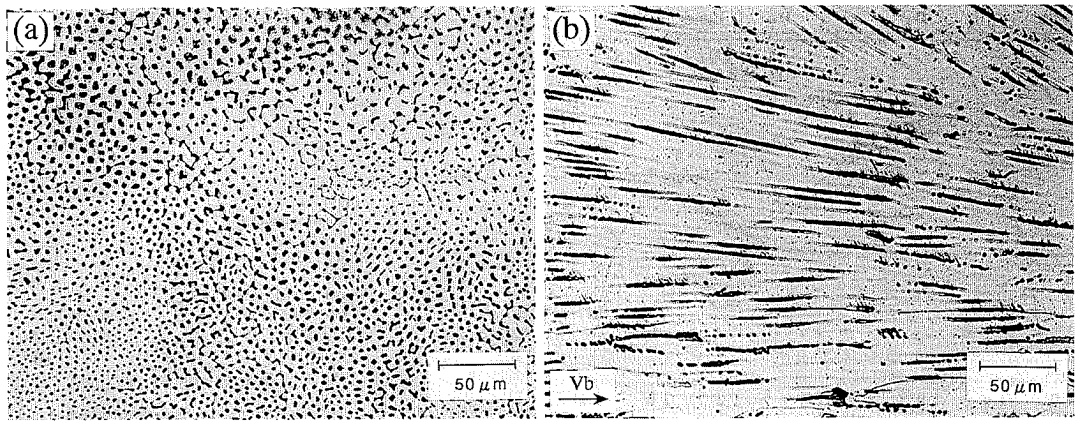

Fig. 8. Eutectic structure observed in laser experiments of alloy C at $V_b = 0.2$ mm/s, (a) transverse section and (b) longitudinal section. Dark phase is ferrite, bright phase is austenite.

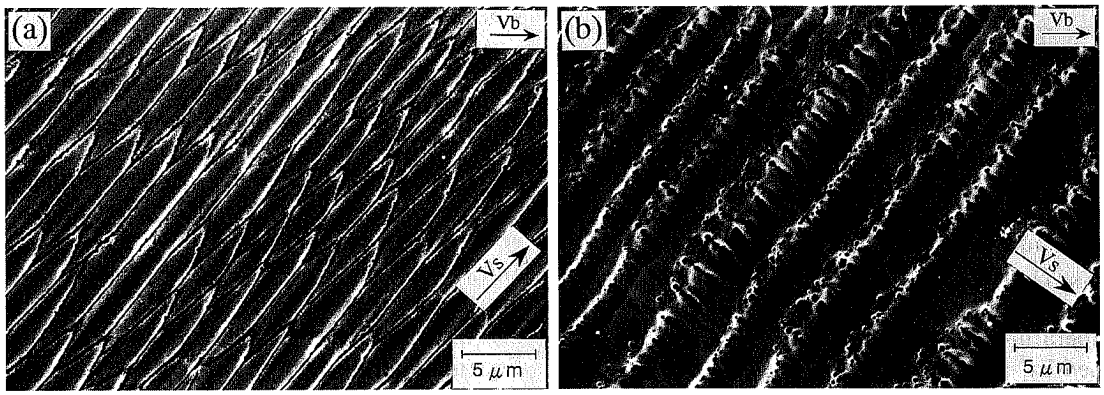

Fig. 9. Microstructures obtained in laser resolidification of alloy B. (a) γ-cellular structure at $V_s = 48$ mm/s and (b) banded structure oscillating between γ-cells and γ-planar front at $V_s = 91$ mm/s.

absorption coefficient by a semi-analytical model and determined the thermal gradient in laser resolidification with similar preheating conditions for Ni–Al alloys to be $G = 500 \pm 250$ K/mm.) It should be noted that the temperature gradient is changed by scanning velocity and the location in the remelted zone.[36] A value of $G = 700$ K/mm was used for the calculations of the laser experiments with preheating of 1 273 K.

A temperature gradient $G = 17 \pm 5$ K/mm in directional solidification was obtained by dendrite arm spacing measurements. The temperature gradient measured in the same apparatus for Fe–Ni alloys was between 10 and 15 K/mm.[37] In this work, the values $G = 15$ K/mm was used for theoretical predictions of the Bridgman experiments.

4.2. Interface Response Functions

Phase selection makes use of interface response functions which for a given G-value describe the growth temperature of all possible morphologies; plane front, cells, dendrites, eutectic. All the equations presented below are for steady state conditions.

4.2.1. Dendrite Growth

Dendrite growth in a positive temperature gradient ahead of dendrite tip such as is observed in Bridgman growth or laser welding can be calculated by current theory,[25,38] which has been extended to multicomponent systems.[19,26] The details of dendrite growth modeling are described in Refs. 26) and 36). Dendrite/cell tip temperature T_d is obtained by

$$T_{d/c} = T_l + \sum (C_i^* m_{v,i} - C_{0,i} m_{0,i}) - 2\Gamma/R - V_s/\mu - GD/V_s \quad \text{.....(1)}$$

$$C_i^* = C_{0,i}/[1-(1-k_{v,i})\mathrm{Iv}(\mathrm{Pe}_i)] \quad \text{.....(2)}$$

where T_l is a liquidus temperature of the initial alloy, C_i^* the liquid concentration at the dendrite tip for constituent i (Cr, Ni), $C_{0,i}$ the initial composition, $m_{v,i}$ the velocity dependent liquidus slope for binary and dilute solution,[47] Γ the Gibbs–Thomson coefficient, R the dendrite tip radius, V_s the dendrite growth velocity, μ a interface kinetic coefficient, G the average thermal gradient, D the solute diffusivity in the liquid assumed to be the same for all alloying elements, $k_{v,i}$ the velocity dependent partition coefficient[39] and $\mathrm{Iv}(\mathrm{Pe}_i)$ the Ivanstov function (a function of Peclet number).

4.2.2. Single Phase Plane Front Growth

The growth temperature of a single phase planar front, T_p is[36,38]

$$T_p = T_s + \sum C_{0,i}(m_{v,i}/k_{v,i} - m_{0,i}/k_{0,i}) - V_s/\mu \quad \text{.....(3)}$$

where T_s is a solidus temperature of the initial alloy.

4.2.3. Simultaneous Two Phase Growth

A model for eutectic growth in ternary alloys has been developed by McCartney *et al.*,[40] the validity of

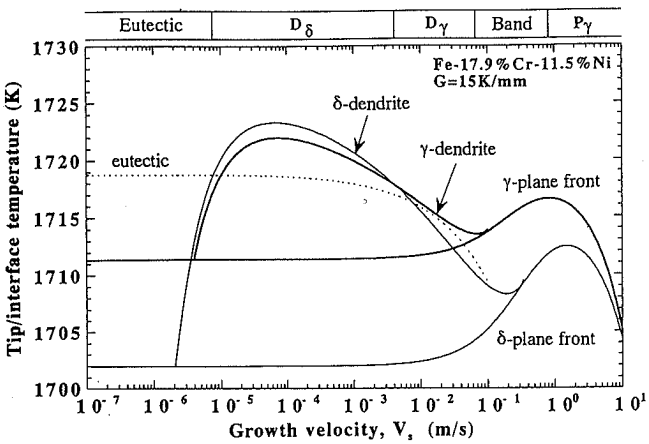

Fig. 10. Interface response functions for δ, γ and eutectic in Fe–17.9%Cr–11.5%Ni alloy (alloy E) with a temperature gradient of $G=15$ K/mm.

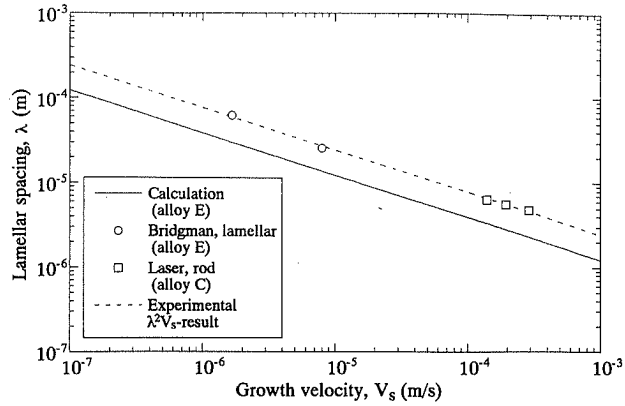

Fig. 11. Comparison between band measured and calculated lamellar spacings as a function of growth rate for alloys C and E.

which is limited to small additions of a third element to a binary eutectic system. Simultaneous two phase growth was therefore treated by a simplified eutectic growth model,[41] which is based upon Jackson–Hunt theory.[42] The solute distributions of both Cr and Ni for two eutectic phases (δ and γ) in the melt ahead of interface for small Peclet numbers were solved with the assumption of $k_{Cr}(\delta)=k_{Ni}(\gamma)=1$. Then the average undercoolings for both solute and curvature were calculated. The growth temperature of simultaneous two phase growth T_e is obtained by

$$T_e = T_{eut} - \Delta T_e \quad \text{.....(4)}$$

$$\Delta T_e = 2(K_r K_c V_s)^{1/2} \quad \text{.....(5)}$$

and the lamellar spacing λ is given by:

$$\lambda = (K_r / V_s K_c)^{1/2} \quad \text{.....(6)}$$

$$K_c = \frac{m_{\delta,Ni} m_{\gamma,Cr}}{m_{\delta,Ni} + m_{\gamma,Cr}} \times \left(\frac{(1-k_{\delta,Ni})(1-f) C_{E,Ni}}{2\pi D_{Ni}} + \frac{(1-k_{\gamma,Cr}) f C_{E,Cr}}{2\pi D_{Cr}} \right) \quad \text{...(7)}$$

$$K_r = \frac{2m_{\gamma,Cr}(1-f)\Gamma_\delta \sin\theta_\delta + 2m_{\delta,Ni} f \Gamma_\gamma \sin\theta_\gamma}{f(1-f) m_{\delta,Ni} m_{\gamma,Cr}} \quad \text{.....(8)}$$

where T_{eut} is the eutectic equilibrium temperature, K_c and K_r are terms due to solute diffusion and curvature, respectively, f is the volume fraction of the δ phase, C_E is the eutectic composition and θ is the contact angle between solid and liquid as defined in Ref. 42).

4.2.4. Prediction of Microstructure and Phase Selection

Figure 10 shows an example of calculated interface response functions for δ, γ and δ–γ eutectic. The data bank of Thermo-Calc[31] version J was used to obtain a consistent thermodynamic description of the phase equilibrium in the stable and metastable ranges. By assuming abundant nucleation of all phases, *i.e.* that the phase with the highest growth temperature is formed, the microstructure/phase selection during solidification can be calculated. (top of Fig. 10)

4.3. Eutectic Growth

According to the phase diagram of the Fe–Cr–Ni system, the composition of the peritectic to eutectic transition of the liquidus line can be located at ~10 mass% Cr and ~7 mass% Ni (Fig.1). Therefore, an eutectic structure is expected to form in the alloys used in this work (Cr≅18%). With an equilibrium volume fraction of δ-ferrite in equilibrium for alloys C and E greater than 0.4, lamellar structures are therefore expected as shown in Figs. 4(a) and 4(b). **Figure 11** shows the measured and calculated lamellar spacings from Eq. (6). The lamellar spacings decrease with increasing growth rate ($\lambda^2 V_s$(exp.) $=5.9\times10^{-15}$ m^3/s) in qualitative agreement with theory ($\lambda^2 V_s$(ther.) $=1.5\times10^{-15}$ m^3/s).

Rod-like eutectic structures were also observed in the present work at high growth rates and temperature gradients. However, it should be noted that it is not always easy to distinguish between rod-type eutectic and intracellular ferrite which results from δ-cell solidification and subsequent δ/γ transformation. The morphology of δ-ferrite during solidification can be altered due to solid state transformation. Generally primary dendrite/cell spacing is twice or three times as large as eutectic rod spacing.[21] Rod-type eutectic microstructures during the directional solidification of Fe–Cr–Ni alloys have also been reported by Okane and Umeda.[21] The eutectic rod mean spacing obtained in their work is similar to the average experimental spacings evaluated in this work.

In Fig. 5, an increase in Cr and a decrease in Ni within the lamellar boundaries was observed. It is caused by δ/γ solid state transformation. The δ phase decreases due to δ/γ transformation as the temperature falls. The δ phase remaining after δ/γ transformationis enriched in Cr and depleted in Ni than before the transformation.

4.4. Banded Structure

Banded structures have been observed in many alloys.[24] These structures are composed of alternate bands which develop parallel to the solidification front. Carrard *et al.*[23] proposed a phenomenological model for this oscillatory instability of the solid–liquid interface. Karma and Sarkassian studied the formation of the banded structure numerically and gave a detailed de-

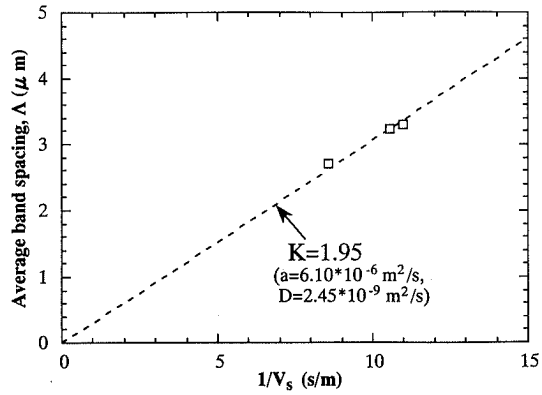

Fig. 12. Relationship between band spacing and reciprocal growth rate for alloy B. Straight line represent $\Lambda V_s = \text{const.}$

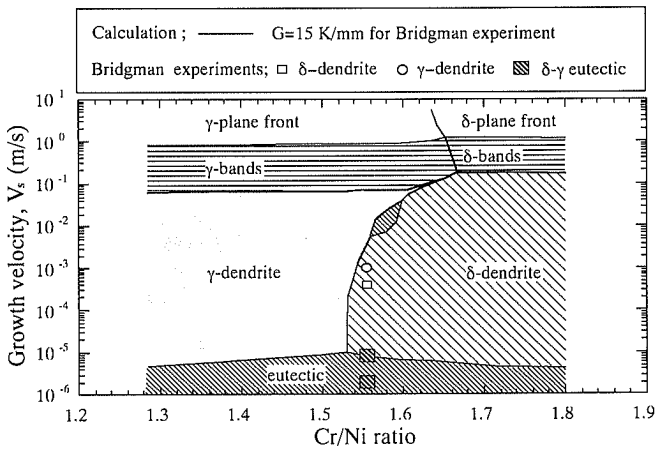

Fig. 13. Solidification microstructure selection map for Fe–18%Cr–Ni alloys with temperature gradient of $G = 15$ K/mm. Theoretical predictions are compared with experimental results.

scription of the interface oscillation.[43,44] They noted that the geometric mean of l_T, the thermal diffusion length ($=a/V_s$) and l_C, the solute diffusion length ($=D/V_s$) is roughly proportional to the total band spacing in their numerical calculation as given by Eq. (9).

$$\Lambda = K\sqrt{l_T l_C} = K\sqrt{aD}/V_s \quad \text{.....(9)}$$

where K is a constant of order unity and a is the thermal diffusivity in the liquid.

Figure 12 shows the relationship between the total band spacing and the inverse of isotherm velocity in this work. The dotted line in Fig. 12 represents a value of K equal to 1.95. Experimental measurements are thus in reasonable agreement with theory.

4.5. Solidification Microstructure Selection Maps

Figure 13 shows the solidification microstructure selection map ($G = 15$ K/mm) in which the experimental results obtained by Bridgman directional solidification experiments are also indicated. Eutectic structure is formed at low growth rates. It is also shown that an increases of the solidification velocity can produce a change of the primary phase from stable ferrite to metastable austenite. The agreement between experimental and predicted microstructure/phase selection map

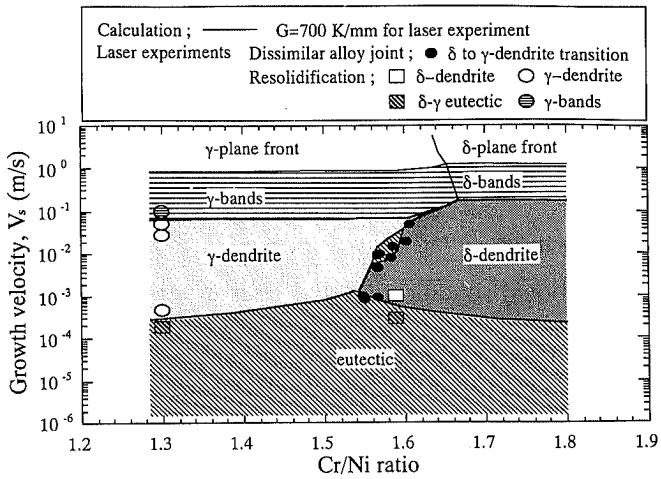

Fig. 14. Solidification microstructure selection map for Fe–18%Cr–Ni alloys with temperature gradient $G = 700$ K/mm. Theoretical predictions are compared with experimental results.

is reasonable. It should be mentioned that the growth velocities over 10 mm/s can not be reached in Bridgman experiments.

Figure 14 shows the calculated solidification microstructure selection map ($G = 700$ K/mm) in comparison with the experimental results obtained by laser experiments. This figure shows various microstructures (dendrite/cell, plane front, eutectic and bands) and phases (δ and γ) according to the compositions and the growth velocities. The calculated transition velocities are in reasonable agreement with experimental results.

In the composition range of this work, eutectic is formed at low growth rates as has been observed earlier.[21] In the case of the Bridgman experiments, the dendritic/cellular regime is expanded into the low velocity range, because smaller G values decrease the limit of constitutional undercooling. The temperature gradient is one of the important factors controlling microstructures at low V_s values. Cell undercooling GD/V_s (fifth term of right-hand side in Eq. (1)) becomes dominant in the low velocity range.[45,46] With increasing growth velocity, the formation of metastable austenite dendrites is favored at the expense of stable ferrite. Banded structure and planar front can be formed at high solidification velocity as shown in Fig. 14.

In both Figs. 13 and 14, calculated δ to γ transitions slightly differ from experimental results. This small deviation may be caused by the other elements, especially Carbon and Nitrogen which greatly affect the solutal undercooling because of small partition coefficients and large absolute liquidus slopes.[16] Cr/Ni-equivalent[7,8,16] can be used instead of Cr/Ni in order to consider the effects of Carbon and Nitrogen on microstructure selection. These are austenite stabilizing elements. Therefore, experimental plots in Figs. 13 and 14 slightly shift to the lower Cr/Ni side by adding the effects of these elements. Better agreement between theoretical predictions and experimental results can be obtained.

In these figures, the formation of eutectic structure is predicted at the medium growth velocity. However, eutectic solidification was not observed in the experi-

ments between $V_s = 5$–50 mm/s. It may be caused by the discrepancy of calculated phase diagram which affects the reference temperature of δ-Fe and γ-Fe and eutectic. Further improvement of the thermodynamic database for Fe–Cr–Ni system is needed to obtain a more accuracy of theoretical predictions.

5. Conclusions

Directional solidification and laser experiments were carried out in Fe–Cr–Ni alloys in order to examine the solidification microstructures and phases. For a wide range of solidification rates, the following results were obtained.

(1) Eutectic structures were observed in both directional solidification and laser experiments. Measured lamellar spacings were in reasonable agreement with calculated ones.

(2) With an increase in growth velocity, γ-dendrites were formed at Cr/Ni $\sim$ 1.30 at the expense of δ–γ eutectic. On the other hand, with increasing growth velocity, δ-dendrites were formed at Cr/Ni $\sim$ 1.59 instead of δ–γ eutectic.

(3) With an increase in growth velocity, metastable γ-dendrites were formed at Cr/Ni $\sim$ 1.56 at the expense of stable δ-dendrites. The transition from δ to γ is controlled by the dendrite growth kinetics. The effect of alloying element, especially Carbon and Nitrogen, can not be neglected for microstructure selection.

(4) A banded structure, oscillating between γ-cell and γ-plane front, was observed in laser treatments at high growth rates. Measured total band spacing was in reasonable agreement with theoretical prediction.

(5) The solidification microstructure selection maps based upon theory is described according to the alloy compositions and growth velocities. Theoretical predictions are compared with experimental results. The agreement between experimental and predicted microstructure selection map is reasonable. It demonstrates the potential of this approach to analyze the microstructure and phase formation as a function of alloy composition and growth conditions. It is thought that further refinement of the thermodynamic data for Fe–Cr–Ni alloys and Cr–Ni stainless steels permits a more precise prediction of microstructure and phase selection.

Acknowledgments

The authors would like to thank Nippon Steel Corporation for financial support. They are grateful to J.-D. Wagnière, J. Stramke and B. Neal for their technical assistance in the laser experiments, in the Bridgman experiments and in the metallographic observations, respectively. Appreciation is expressed to Drs. M. Vandyoussefi and O. Hunziker for valuable discussions. One of the authors (SF) acknowledges the help of Y. Matsumoto, Nippon Steel Corporation, in the SEM observations. Appreciation is also expressed to Prof. T. Umeda, the University of Tokyo, for valuable comments.

REFERENCES

1) K. Kujanpaa, N. Suutala, T. Takalo and T. Mioiso: *Weld. Res. Int.*, **9** (1779), 55.
2) S. Katayama, T. Fujimoto and A. Matsunawa: *Trans. JWRI*, **14** (1985), 123.
3) J. A. Brooks and A. W. Thompson: *Int. Mater. Rev.*, **36** (1991), 16.
4) A. L. Schaeffler: *Met. Prog.*, **56** (1949), 680.
5) W. T. DeLong, G. A. Ostrom and E. R. Szumachowski: *Weld. J.*, **35** (1956), 526s.
6) F. C. Hull: *Weld. J.*, **52** (1973), 193s.
7) O. Hammer and U. Svensson: Solidification and Casting of Metals, The Metals Society, London, (1979), 401.
8) N. Suutala: *Metall. Trans.*, **13A** (1982), 2121.
9) N. Suutala: *Metall. Trans.*, **14A** (1983), 191.
10) S. Katayama and A. Matsunawa: *L. I. A.*, **44** (1984), ICALEO, 60.
11) S. A. David, J. M. Vitek and T. L. Hebble: *Weld. J.*, **66** (1987), 289s.
12) Y. Nakao, K. Nishimoto and W. Zhang: *Q. J. Jpn. Weld. Soc.*, **7** (1989), 414.
13) J. W. Elmer, S. M. Allen and T. W. Eager: *Metall. Trans.*, **20A** (1989), 2117.
14) J. A. Brooks, M. I. Baskes and F. A. Greulich: *Metall. Trans.*, **22A** (1991), 915.
15) S. Fukumoto and W. Kurz: *ISIJ Int.*, **37** (1997), 677.
16) S. Fukumoto and W. Kurz: *ISIJ Int.*, **38** (1998), 71.
17) W. Kurz and R. Trivedi: Trends in Welding Research, ed. by H. B. Smartt, J. A. Johnson and S. A. David, ASM, Metals Park, OH, (1996), 115.
18) T. Umeda, T. Okane and W. Kurz: *Acta Mater.*, **44** (1996), 4209.
19) M. Bobadilla, J. Lacaze and G. Lesoult: *J. Cryst. Growth*, **89** (1988), 531.
20) H. K. D. H. Bhadeshia, S. A. David and J. M. Vitek: *Mater. Sci. Technol.*, **9** (1991), 50.
21) T. Okane and T. Umeda: *ISIJ Int.*, **38** (1998), 454.
22) M. Gremaud, M. Carrard and W. Kurz: *Acta Metall.*, **39** (1991), 1431.
23) M. Carrard, M. Gremaud, M. Zimmermann and W. Kurz: *Acta Mater.*, **40** (1992), 983.
24) W. Kurz and R. Trivedi: Metall. *Mater. Trans.*, **27A** (1996), 625.
25) W. Kurz, B. Giovanola and R. Trivedi: *Acta Metall.*, **34** (1986), 823.
26) M. Rappaz, S. A. David, J. M. Vitek and L. A. Boatner: *Metall. Trans.*, **21A** (1990), 1767.
27) P. Gilgien, A. Zryd and W. Kurz: *ISIJ Int.*, **35** (1995), 566.
28) S.C. Gill and W. Kurz: *Acta Mater.*, **41** (1993), 3563.
29) O. Hunziker and W. Kurz: *Acta Mater.*, **45** (1997), 4981.
30) M. Vandyoussefi, H. W. Kerr and W. Kurz: Proc. Int. Conf. Solidification Processing, ed. by J. Beech and H. Jones, University of Sheffield, UK, (1997), 564.
31) B. Sundman, B. Jansson and J.-O. Andersson: *CALPHAD*, **9** (1985), 153.
32) T. Takalo, N. Suutala and T. Moisio: *Metall. Trans.*, **10A** (1979), 1173.
33) A. F. A. Hoadley, M. Rappaz and M. Zimmermann: *Metall. Trans.*, **22A** (1991), 101.
34) J. W. Elmer: The Metals Science of Joining, TMS, Warrendale, PA, (1992), 123.
35) H. Esaka, S. Mizoguchi, H. Kajioka and H. Senda: *CAMP-ISIJ*, **1** (1988), 268.
36) R. Trivedi and W. Kurz: *Int. Mater. Rev.*, **39** (1994), 49.
37) M. Vandyoussefi, H. W. Kerr and W. Kurz: *Acta Mater.*, **45** (1997), 4093.
38) W. J. Boettinger, S. R. Coriell and R. Trivedi: Rapid Solidification Processing, Principles and Technologies, ed. by R. Mehrabian and P. A. Parrish, Claitor's Publ. Div., Baton Rouge, LA, (1988), 13.
39) M. J. Aziz: *J. Appl. Phys.*, **53** (1982), 1158.
40) D. G. McCartney, J. D. Hunt and R. M. Jordan: *Metall. Trans.*, **11A** (1980), 1251.

41) W. Kurz and D. J. Fisher: Fundamentals of Solidification, Trans. Tech. Publications, Aedermannsdorf, Switzerland, (1989), 261.
42) K. A. Jackson and J. D. Hunt: *Trans. AIME*, **236** (1966), 1129.
43) A. Karma and A. Sarkassian: *Phys. Rev. E*, **47** (1993), 513.
44) A. Sarkissian and A. Karma: *Mater. Sci. Eng. A*, **178** (1994), 153.
45) M. H. Burden and J. D. Hunt: *J. Cryst. Growth*, **22** (1974), 109.
46) T. F. Bower, H. D. Brody and M. C. Flemings: *Trans. Metall. Soc. AIME*, **236** (1966), 624.
47) W. J. Boettinger and S. R. Coriell: Science and Technology of the Undercooled Melt, ed. by P. R. Sahm, H. Jones and C. M. Adams, Martinus Nijhoff Publication, Dordrecht, (1981), 81.
48) H. Mizukami, T. Suzuki, T. Umeda and W. Kurz: *Mater. Sci. Eng.*, **A177** (1993), 361.
49) T. Koseki and M. C. Flemings: *Metall. Mater. Trans.*, **28A** (1997), 2385.
50) T. Koseki and M. C. Flemings: *Metall. Mater. Trans.*, **26A** (1995), 2991.
51) T. Volkmann, W. Loser and D. M. Herlach: *Metall. Mater. Trans.*, **28A** (1997), 453.
52) T. Volkmann, W. Loser and D. M. Herlach: *Metall. Mater. Trans.*, **28A** (1997), 461.